



Temperature dependence of thermal resistance at the water/silicon interface



Murat Barisik*, Ali Beskok

Southern Methodist University, Lyle School of Engineering, Mechanical Engineering Department, Dallas, TX 75275-0337, USA

ARTICLE INFO

Article history:

Received 4 April 2013

Received in revised form

16 October 2013

Accepted 17 October 2013

Available online

Keywords:

Kapitza resistance

Nano-scale heat transfer

Phonon transport

Molecular dynamics

ABSTRACT

Molecular dynamics (MD) simulations of heat transport through a water–silicon system are performed to investigate the thermal resistance at water/silicon interface. Interaction strength between water and silicon is varied in order to understand its effects while the proper strength value is characterized by matching the nano-scale contact angle value with the micro-scale experimental measurements through a water droplet study. Depending on surface wettability, different water distributions are developed near the surface, creating different couplings between water and silicon molecules for phonon transport. In addition, near surface water density is found to be dependent on the surface temperature for high wetting cases that closer packing of water molecules is observed near the cold surface. Interface thermal resistance values measured as Kapitza length (L_K) showed strong dependence on water density structure formed next to the surface. Hence, variation of L_K with temperature is not only measured due to the temperature dependence of phonon transport, but also due to the variation of near surface density with temperature. For studied water/silicon system (slightly hydrophobic with contact angle of 88°), density is independent of surface temperature, and L_K decreases with increased temperature similar to the theoretical phonon transport predictions. MD predicted L_K values (≈ 9 nm) are found to be consistent with experimental measurements.

© 2013 Elsevier Masson SAS. All rights reserved.

1. Introduction

Heat transfer through two dissimilar materials is interrupted due to a temperature jump at the interface. From the phonon transport perspective, Mismatch Models explains such behavior as the deficiency in overlap between phonon dispersions of different materials. The Acoustic Mismatch Model (AMM) and the Diffuse Mismatch Model (DMM) have been used for theoretical considerations of the interface phonon transport [1,2]. AMM neglects phonon scattering at the interface and predicts high interface thermal resistance (ITR); while DMM considers diffuse scattering of phonons on the interface and yields low resistance. Hence, these two models gives the upper and lower limits of ITR [3], while detailed investigation of intermolecular interactions is needed for a better understanding of the interface phonon scattering mechanisms.

Phonon transport is classically studied by lattice dynamics based on harmonic wave theory in the frequency space. However,

the anharmonic behaviors forming in a crystal structure cannot be described with this theory. Alternatively, the coupled motions of the atoms in real space can be modeled by Molecular Dynamics (MD) which provides the natural formation and transport of phonons via vibrations in the crystal lattice. As a result, MD has been utilized to investigate phonon transport through the interfaces [3–21]. There are quite a number of studies revealing the dependence of ITR to various molecular parameters; but the effect of surface temperature on ITR is still a question. For a solid/solid interface, it was validated that the temperature dependence of ITR is similar to the theoretical predictions where increase of temperature enhances the phonon density of states and decreases the ITR [19]. However, in the case of a solid/liquid interface, liquid molecular structure formed near the surface plays a dominant role on the interface phonon transport. Opposite to the theoretical expectations, our earlier studies showed increase of ITR with increased temperature [4–7]. Such behavior develops as a result of the temperature dependence of liquid density layering. For the studied monatomic liquid argon in contact with silver [6,7] and solid argon surfaces [4,5], liquid density was found to be higher and better packed near the cold surface; as a result, the ITR was lower than the hot side. Hence, correct characterization of temperature

* Corresponding author. Tel.: +1 (214) 768 3200.

E-mail address: mbarisik@smu.edu (M. Barisik).

dependence of ITR needs a detailed investigation of near surface liquid structure whose dependence on temperature shows variation for surfaces having different wetting behavior.

A liquid near a solid surface exhibits layering on the molecular scale due to the ordering of the liquid molecules under the influence of surface forces [22]. This density layering is a specific property of a liquid/solid couple and develops mainly as a function of the surface wettability driven by the intermolecular interactions. However, the parameters determining the interactions of the specific liquid/solid couples are still under investigation. Frequently, the interaction parameters of non-identical molecules are calculated from parameters of the pair of identical molecules by using the Lorentz–Berthelot mixing rule. However, the interaction parameters between identical molecules are optimized for a bulk material system and may need to be re-parameterized for the interaction of non-identical pairs instead of using the simple Lorentz–Berthelot mixing rule. Therefore, the intermolecular interaction parameters should be properly specified in order to capture the correct behavior of ITR for a given solid/liquid couple.

The objective of this study is to predict the interface thermal resistance between silicon and water for the case where the interaction parameters are properly tuned to capture the hydrophobic behavior of bare silicon surface. In the mean time, an enhanced understanding of the near wall density structure influences on ITR and its dependence on the surface temperature will be provided.

This paper is organized as follows: In Section 2, we described MD simulation details of silicon–water system. In Section 3, we studied the effects of near wall density structure on ITR for different interaction strength values. Detailed comparisons are made on density profiles near the hot and cold surface of each case to reveal the temperature dependence of water layering at different surface wettability values. In Section 4, we specified the interaction strength between water and silicon by matching the macroscopic wetting behavior of water on silicon and studied the temperature dependence of ITR. In the conclusions section, the proper LJ parameters for recovering the macroscopic wetting behavior of water on silicon and the resulting Kapitza length are presented.

2. Three-dimensional MD simulation details

Liquid water is confined between two parallel solid silicon walls as illustrated in Fig. 1. Total dimensions in longitudinal (x), vertical (y), and lateral (z) directions are 13.4, 2.7 and 2.7 nm, respectively. The domain was constructed using 2500 Silicon and 1696 Water molecules while the corresponding density of water is $\rho = 1.006 \text{ g/cm}^3$. Walls on each side of the domain contain 25 Silicon layers, which are 0.136 nm apart from each other, and the spacing between two silicon walls is 6.4 nm in x -direction. Periodic boundary conditions are applied in the vertical (y) and lateral (z) directions.

Table 1
Molecular interaction parameters utilized.

| Molecule pair | σ (Å) | ϵ (eV) | q (e) |
|---------------|--------------|-----------------|---------|
| O–O | 3.166 | 0.006739 | –0.8476 |
| H–H | 0 | 0 | +0.4238 |
| Si–Si | 2.095 | 2.168201 | 0 |

Silicon surface is modeled as diamond cubic structure with (0,0,1) crystal plane facing the fluid. Atoms in the outmost layer of both silicon walls are fixed to their original locations to maintain a fixed volume system, while the remaining atoms throughout the domain are free to move.

We used the SPC/E water model which is described as effective rigid pair potentials composed of Lennard–Jones and Coulombic terms [23]. This water model has three interaction sites, corresponding to the three atoms of the water molecules. Each atom gets assigned a point charge to model the long-range Coulombic interactions, and the oxygen atom also exhibits Lennard–Jones potential to model van der Waals forces. The truncated (6–12) Lennard–Jones (L–J) potential is given as,

$$\Phi_{\text{truncated}}(r_{ij}) = 4e \left(\left(\left(\frac{\sigma}{r_{ij}} \right)^{12} - \left(\frac{\sigma}{r_{ij}} \right)^6 \right) - \left(\left(\frac{\sigma}{r_c} \right)^{12} - \left(\frac{\sigma}{r_c} \right)^6 \right) \right), \quad (1)$$

where r_{ij} is the intermolecular distance, ϵ is the depth of the potential well, σ is the molecular diameter and r_c is the cut-off radius [24].

SPC/E is a tetrahedral model with an OH bond length of 0.1 nm and H–O–H angle of 109.47°. SHAKE algorithm [25] is used to constrain the bond lengths and angle, thus making the model rigid. A short-range Lennard–Jones term with a cut-off distance of 1 nm acts on the oxygen, while a charge q (0.4238e) is on each hydrogen, compensated by a charge $-2q$ (–0.8476e) on the oxygen. The long-range Coulombic part has been treated with a particle–particle particle-mesh (PPPM) solver which can handle long-range interactions for periodic systems with slab geometry more efficiently than the Ewald sum algorithm [26]. PPPM invokes a particle–particle particle-mesh solver, which maps atom charge to a 3D mesh. It uses 3D fast Fourier transforms to solve Poisson’s equation on the mesh, and then interpolates electric fields on the mesh points back to the atoms. Si–Si interactions were calculated by Stillinger–Weber potential which considers two-body interactions with an additional many body dependence [27]. SPC/E water molecules interact with silicon surface only by van der Waals interactions of silicon and oxygen using a cutoff distance of 1 nm. The molecular interaction parameters are given in Table 1. For the silicon–oxygen interactions, parameters can be calculated by the Lorentz–Berthelot (L–B) mixing rule given as,

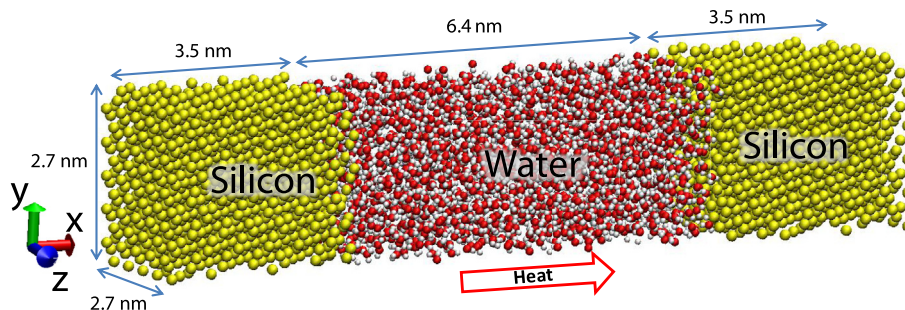


Fig. 1. Snapshot of the simulated Water–Silicon system.

$$\sigma_{\text{Si-O}} = \frac{\sigma_{\text{Si-Si}} + \sigma_{\text{O-O}}}{2}, \quad \epsilon_{\text{Si-O}} = \sqrt{\epsilon_{\text{Si-Si}} \times \epsilon_{\text{O-O}}} \quad (2)$$

Using the corresponding parameters given in Table 1, the L–B mixing rule predicts the interaction parameters $\sigma_{\text{Si-O}}^* = 2.6305 \text{ \AA}$ and $\epsilon_{\text{Si-O}}^* = 0.12088 \text{ eV}$.

Newton's equations of motion were integrated using the Verlet algorithm with a time step of 0.001 ps. We use LAMMPS (Large-scale Atomic/Molecular Massively Parallel Simulator) [28] as our MD solver. Simulations were started from the Maxwell–Boltzmann velocity distribution for all molecules at 323 K. NVT ensemble was applied with Nose Hoover thermostat keeping the system at 323 K. Initial particle distribution was evolved 2×10^6 time-steps (2 ns) to reach an isothermal steady state. Afterward, the Nose Hoover thermostat is applied only on the outmost second, third and fourth layers of the both silicon slabs to induce heat flux through the liquid/solid interfaces by maintaining different wall temperatures. At the same time, NVE ensemble is applied to the remaining silicon and water molecules. Simulations are performed for an additional 4×10^6 time-steps (4 ns) to ensure that the system attains equilibrium in presence of the heat flux. After which, time averaging of desired properties are performed through 24×10^6 additional time steps (24 ns).

Classically, energy fluctuation in an NVT system of a limited number of molecules is nonzero. In such case, increase of the averaging time decreases the fluctuations to a minimum value. This minimum value is a function of multiple molecular parameters, but mostly depends on the time scales of the molecular mechanisms that are modeled. We performed 20 ns averaging which is considered excessively long for a classical MD system. However, the phonon transport in our system occurs at different frequencies. Depicting time-averaged behavior of low frequency phonons require excessively long simulation times that are computationally unfeasible. Further complexity develops due to the phonon scattering at the interface, which makes theoretical estimation of the time scale for the complete phonon spectra impossible. Overall, the fluctuations are mainly dependent on $\epsilon_{\text{Si-O}}$ and the specified temperature difference, where high $\epsilon_{\text{Si-O}}$ values and large temperature differences in the system result in lower fluctuations. Although the highest fluctuations in the temperature and density profiles are less than 2% and 1%, respectively, these variations result in higher fluctuations ($\approx 9\%$) in the ITR calculations. Due to these fluctuations, we performed statistical analysis of our results and report the ITR behavior with corresponding standard deviations (See Section 3 for details).

The computational domain is divided into 100 slab bins with the size of 0.1343 nm for temperature and 200 slab bins with the size of 0.0672 nm for density profiles. Smaller bin size, 800 slab bins with the size of 0.0168 nm, is also employed in order to resolve the fine details of the near wall water density distributions.

Irving–Kirkwood (I–K) expression is utilized to compute the heat flux vector for an N particle system using unity differential operator approximation as follows [29,30],

$$J_k = \frac{1}{\text{Vol}} \left\langle \sum_i^N V_k^i (E^i + \Phi^i) + \sum_{ij}^N (r_k^j + r_k^i) W^{ij} \right\rangle, \quad (3)$$

$$E^i = \frac{1}{2} m^i \left((V_x^i)^2 + (V_y^i)^2 + (V_z^i)^2 \right), \quad (4)$$

$$W^{ij} = \frac{1}{2} \left(V_x^i f_x^{ij} + V_y^i f_y^{ij} + V_z^i f_z^{ij} \right), \quad (5)$$

where the first term on the right hand side of Equation (3) is the kinetic and potential energies carried by particle i , and the second

term is the energy transfer to particle i by force interactions with the surrounding particles. In the first term, V_k^i is the peculiar velocity component of particle i in k -direction, while k is the axes of the Cartesian coordinate system; E^i is the kinetic and Φ^i is the potential energy of particle i calculated using Equations (4) and (1), respectively. In the second component of Equation (3), $(r_k^j - r_k^i)$ is the k th component of the relative distance vector between particles i and j . The W^{ij} term is given in Equation (5), where f_l^{ij} is the intermolecular force exerted on particle i by particle j in the Cartesian coordinate direction l . An overall heat flux is calculated in the water volume using Equation (3) by considering the contributions of each atom within a water molecule.

3. Influence of the near wall water density structure on ITR

In an earlier study [31], we investigated the effect of interaction parameters, specifically interaction strength, to the wetting angle of water on silicon surface. We decreased the interaction strength value starting from the classical mixing rules estimation, and observed transition from hydrophilic to hydrophobic behavior in the studied range. Decrease in the interfacial energy leads lower wetting; and hence, the water density distribution near the surface changes drastically. In this study, we further investigate effect of the interaction parameter to the ITR. For such purpose, we used the $\epsilon_{\text{Si-O}}$ values of 0.4, 0.2, 0.125, 0.1 and $0.05 \times \epsilon_{\text{Si-O}}^*$ where the $\epsilon_{\text{Si-O}}^*$ is the value calculated by the L–B rule ($\epsilon_{\text{Si-O}}^* = 0.12088 \text{ eV}$). Our main purpose here is not only to understand the influence of the resulting near surface fluid structure to the ITR, but also to reveal the importance of the interaction parameter values; since some of the interaction strength values used in this work is similar to the values utilized in previous investigations of ITR using silicon–SPC/E water model [15–17].

Temperature distributions obtained in a silicon–water–silicon system subjected to 353 K and 293 K on its ends are shown in Fig. 2. The temperature profiles vary with the change of interaction strength value. For silicon domain, we observed a temperature drop at the interface of the thermostat applied and thermostat free regions. This artificial ITR created by the thermostat is due to the dynamic rescaling of thermostat which results in phonon mismatch at this interface. This artificial effect of the thermostat was investigated earlier [6]. Nose Hoover thermostat creates temperature gradient inside the thermostat applied region different than the temperature gradient of the thermostat free domain depending on the temperature and heat flux of the system which was previously investigated in detail [6]. The remaining 21 silicon layers

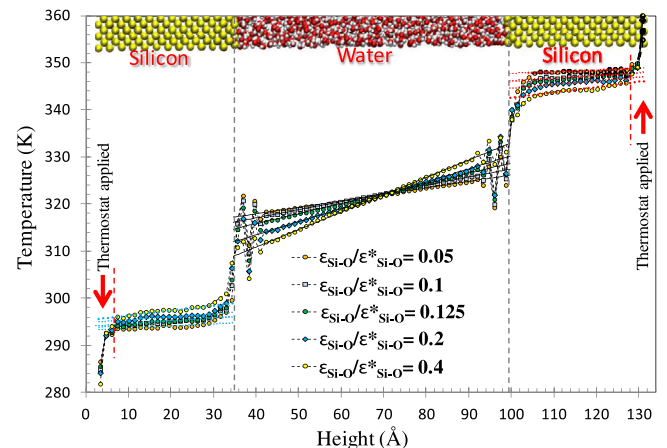


Fig. 2. Temperature profiles of the Silicon–Water–Silicon system at different $\epsilon_{\text{Si-O}}$ values while hot and cold reservoirs are kept at 353 K and 293 K, respectively.

Table 2
Kapitza lengths at hot (L_{K-H}) and cold (L_{K-C}) surfaces, heat flux, temperature gradients and thermal conductivity of liquid water for five different interaction strength values. Hot and cold reservoirs are kept at 353 K and 293 K, respectively. Contact angles for the corresponding interaction strengths are adopted from a water nano-droplet study in Ref. [31].

| Case | ϵ_{Si-O} (eV) | $\epsilon_{Si-O}/\epsilon^*_{Si-O}$ | Contact angle ($^\circ$) [31] | q_x (W/m 2) | dT/dx (K/Å) | k_{water} (W/K m) | T_H (K) | L_{K-H} (nm) | T_C (K) | L_{K-C} (nm) |
|------|------------------------|-------------------------------------|---------------------------------|-------------------|---------------|---------------------|-----------|----------------|-----------|----------------|
| 1 | 0.048352 | 0.4 | 46.3 | 7.712 | 0.369 | 0.690 | 344.4 | 2.977 | 297.3 | 2.687 |
| 2 | 0.024176 | 0.2 | 57.8 | 5.691 | 0.281 | 0.67 | 345.8 | 5.263 | 296.1 | 5.119 |
| 3 | 0.01511 | 0.125 | 108.9 | 4.286 | 0.215 | 0.659 | 347 | 8.186 | 295.1 | 8.878 |
| 4 | 0.012088 | 0.1 | 129.7 | 3.588 | 0.173 | 0.684 | 347.1 | 10.597 | 295.1 | 11.57 |
| 5 | 0.006044 | 0.05 | 169.3 | 2.883 | 0.137 | 0.694 | 348.3 | 14.785 | 294.1 | 16.261 |

interacting freely develop their own temperature profile based on the phonon characteristic of silicon. Silicon temperature varies linearly sufficiently away from the interface. We observed non-linear behavior near the interface extending ≈ 0.54 nm into the silicon slab for the highest heat flux case. Such behavior is a strong evidence of phonon scattering mechanism from the interface which needs further attention and will be investigated in detail in a separate study.

There are sudden temperature jumps at the liquid/solid interfaces. These temperature jumps are due to the mismatch in phonon spectrum of the water–silicon pair and results in the ITR. One can define a thermal resistance length (L_K), known as the Kapitza length, by extrapolating the temperature profile from liquid in to the solid, where the wall temperature is reached. The Kapitza length can be predicted using,

$$\Delta T = L_K \left. \frac{\partial T}{\partial n} \right|_{\text{liquid}}, \quad (6)$$

where $\partial T/\partial n$ is the thermal gradient on the liquid side, and $\Delta T = T_{\text{liquid}} - T_{\text{wall}}$. It is crucial to realize that Equation (6) requires onset of continuum behavior where a local temperature profile can be defined. In order to characterize the temperature distribution in the bulk of liquid water, we performed linear least square fits to the MD data, and measured sum of the squares of the residual, which is a measurement of how well the least square fit represents the data. The values are all below 1%, indicating that the temperature profile is linear in the bulk of the channel. Slight curvature in the temperature profile can be attributed to the temperature dependence of water's thermal conductivity. Water temperature varies linearly except the near wall region where temperature fluctuates as a result of density layering formed due to the surface forces. Such behavior depends on the chosen bin size. While we presented fine distribution with 0.1343 nm bin size (100 bins), a slight increase in the bin size to 0.2686 nm (50 bins) resulted in linear behavior up to very near surface region (≈ 0.15 nm away from surface). We discussed in an earlier study that in order to recover continuum behavior in such small environments, employed bin size should be equal to or bigger than one molecular diameter [4,5].

Next, we calculate the Kapitza length, L_K , by using Equation (6). First we obtained the local temperature gradient from the MD results, and matched this with the slope of the linear curve fits to the temperature profiles in the bulk of the channel. Then, we extrapolated the liquid temperature onto the solid surface, which was assumed to be the center of the last silicon layer facing the liquid; and calculated the local temperature jump ($\Delta T = T_{\text{liquid}} - T_{\text{wall}}$). As suggested by Equation (6), this temperature jump and the linear slope of water temperature profile yield the value of L_K . In the mean time, we also calculated the heat flux using Equation (3), and utilized the temperature gradient obtained from MD result to calculate the thermal conductivity of confined water using Fourier law. Calculated thermal conductivity for liquid water at average temperature of 323 K is ≈ 0.68 W/K m, which matches the published bulk values well [32]. The calculated Kapitza lengths at hot (L_{K-H})

and cold (L_{K-C}) surfaces, heat flux, temperature gradients and thermal conductivity of liquid water are given in Table 2 for five different interaction strength values.

In the studied system, phonon transport that propagates inside the silicon domain at different wavelengths creates thermal fluctuations. As a result L_K cannot converge to a precise value. In order to have a fair judgment on L_K behavior, we performed a statistical investigation of L_K variation. Using a total simulation time of 24 ns, we obtained time averages at every 2 ns, 4 ns, 8 ns and 24 ns, resulting in 12, 6, 3 and 1 data sets, respectively. Using these total 22 differently averaged temperature profiles, 22 different L_K values are calculated. Later, the standard deviation of L_K and surface temperatures are calculated while the reported L_K value is the mean of the 22 L_K values. Standard deviations of the L_K values are given in Fig. 3 as error bars. Overall, fluctuation of L_{K-H} is higher than L_{K-C} . Also standard deviation increases with decreased ϵ_{Si-O} while the highest value of SD is around 7%.

The increase of interaction strength creates better coupling between the water and silicon molecules, and hence, decreases the ITR and L_K values. Variation of L_K values for different $\epsilon_{Si-O}/\epsilon^*_{Si-O}$ at hot and cold surfaces are given in Fig. 3a. Surface temperatures are also indicated on the plot. Since the temperature difference through the system is specified by the thermostat and fixed in the studied system, decrease of ITR results in increase of developed heat flux value. Regardless of this, resulted hot surface temperatures and cold surface temperatures for different ϵ_{Si-O} cases are very close to each other ($T_H \approx 347$ K and $T_C \approx 295$ K). Measured L_K values at cold and hot surface are found to be different. Since the L_K values of different ϵ_{Si-O} cases are different, we decided to normalize the L_{K-H} with L_{K-C} of the corresponding ϵ_{Si-O} case in order to understand the difference of L_{K-H} and L_{K-C} for each case (Fig. 3b). While the L_K measured on the hot surface is lower than the cold surface values for $\epsilon_{Si-O} < 0.2 \times \epsilon^*_{Si-O}$, we observed higher L_{K-H} than L_{K-C} for larger ϵ_{Si-O} cases. The interesting behavior of L_{K-H} and L_{K-C} for different ϵ_{Si-O} cases clearly indicates that L_K at a liquid/solid interface is not dominated by the surface temperature.

Next, we investigate the water and silicon density profiles in Fig. 4 which illustrates the system consisting of three distinct domains. A constant silicon density of 2.35 g/cm 3 is observed. Water density is constant and equal to 1.006 g/cm 3 in the bulk of the channel. Near surface water density exhibits well known density layering due to the surface forces and local water–water interactions [31]. Increase in the interaction strength develops stronger water layering for $\epsilon_{Si-O} \geq 0.2 \times \epsilon^*_{Si-O}$, while the increase in the near wall water density results in slight decrease of density in the bulk. By simple examination of Fig. 4, one can conclude that the water density peaks near the hot surface are higher than the cold side for $\epsilon_{Si-O} \geq 0.2 \times \epsilon^*_{Si-O}$. However, a more detailed investigation should be conducted to understand the behavior of water density near the surface and the effects near wall density distribution on the ITR.

Water density variations near the hot and cold reservoirs are shown in Fig. 5 using finer bin size of 0.0168 nm for various ϵ_{Si-O} values. Similar to our earlier study, water penetration into the

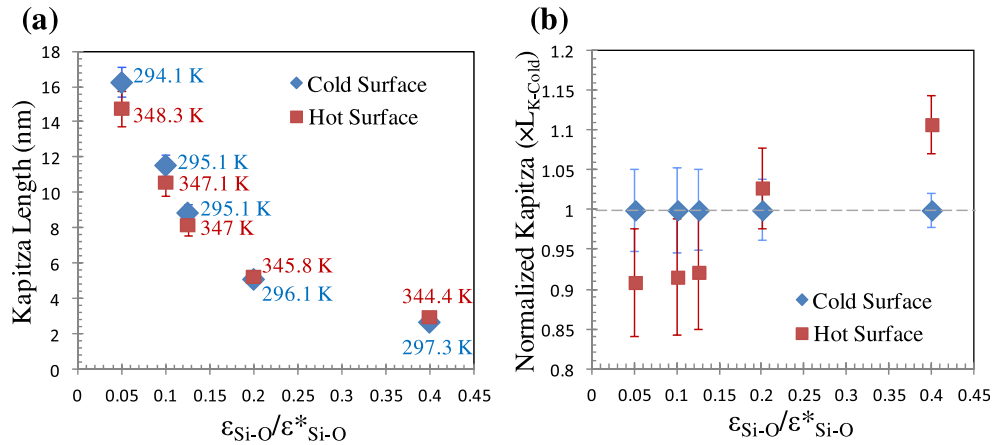


Fig. 3. (a) L_K values for different $\epsilon_{\text{Si-O}}/\epsilon_{\text{Si-O}}^*$ ($\epsilon_{\text{Si-O}}^* = 0.12088$ eV) cases obtained at hot and cold surfaces. Surface temperatures are also given on the plot. (b) Variation of the hot wall L_K value normalized with the corresponding cold surface L_{K-C} value for different $\epsilon_{\text{Si-O}}/\epsilon_{\text{Si-O}}^*$ cases.

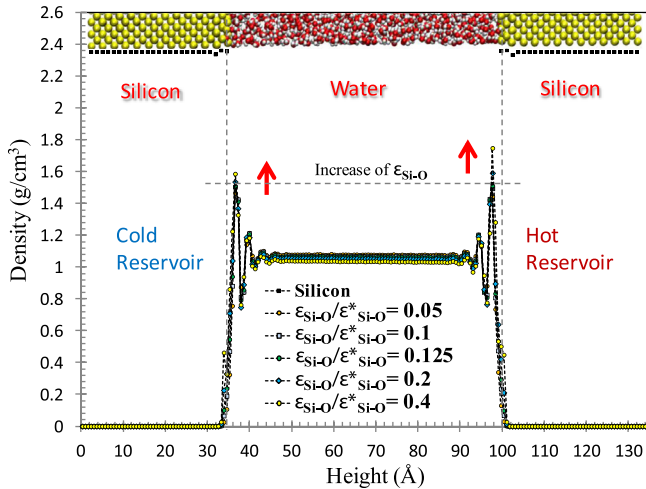


Fig. 4. Density profiles of the Silicon–Water–Silicon system at different $\epsilon_{\text{Si-O}}$ values while hot and cold reservoirs are kept at 353 K and 293 K, respectively.

gap between the first and second silicon layers is observed, and the water density in this region increases with increased $\epsilon_{\text{Si-O}}$. There also forms an additional density layer between the first density peak of water and silicon surface while these two density behaviors become profound for $\epsilon_{\text{Si-O}} \geq 0.2 \times \epsilon_{\text{Si-O}}^*$. These two new density layers are indicated with arrows in Fig. 5c. Simply, decrease of ITR with an increased $\epsilon_{\text{Si-O}}$ is the results of the stronger coupling between water and silicon molecules due to closer interactions. Comparisons of hot and cold side water densities of each case are also shown in Fig. 5a–d. Water distributions near the hot and cold surfaces are identical for low $\epsilon_{\text{Si-O}}$ values ($\epsilon_{\text{Si-O}} < 0.2 \times \epsilon_{\text{Si-O}}^*$). Starting with the $0.2 \times \epsilon_{\text{Si-O}}^*$ case, the additional density layer near the surface is more prominent at the cold side, which creates a better phonon coupling resulting in the L_{K-C} value being lower than L_{K-H} . While the densities for the $\epsilon_{\text{Si-O}} < 0.2 \times \epsilon_{\text{Si-O}}^*$ cases show no dependency on the surface temperature, density becomes more packed with decreased surface temperature for $\epsilon_{\text{Si-O}} \geq 0.2 \times \epsilon_{\text{Si-O}}^*$, which decreases the ITR. Thus, in Fig. 3b, we observed not only the variation of ITR with temperature but also the temperature dependency of the water density, which affects the ITR value.

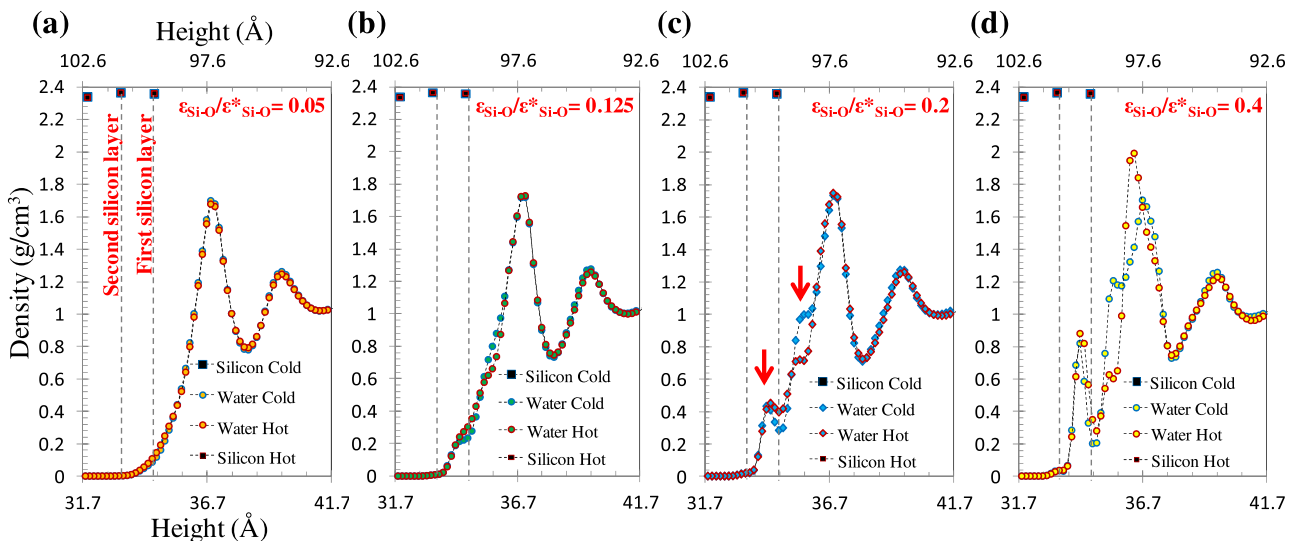


Fig. 5. (a–d) Comparison of the density distribution near the hot and cold surfaces for various $\epsilon_{\text{Si-O}}/\epsilon_{\text{Si-O}}^*$ cases.

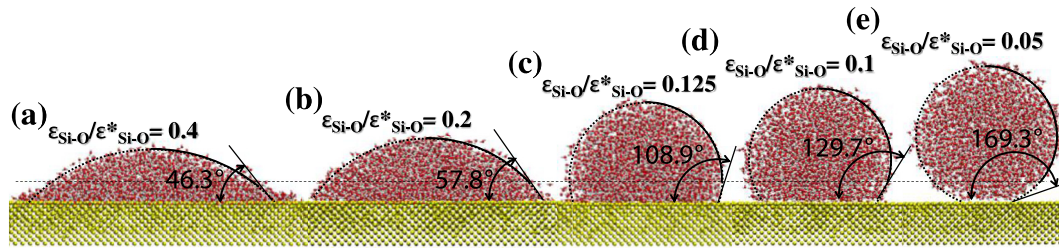


Fig. 6. (a–e) Snapshot of the nano-scale water droplets formed on bare (1,0,0) silicon surface and microscopic contact angle values at the corresponding interaction strength values.

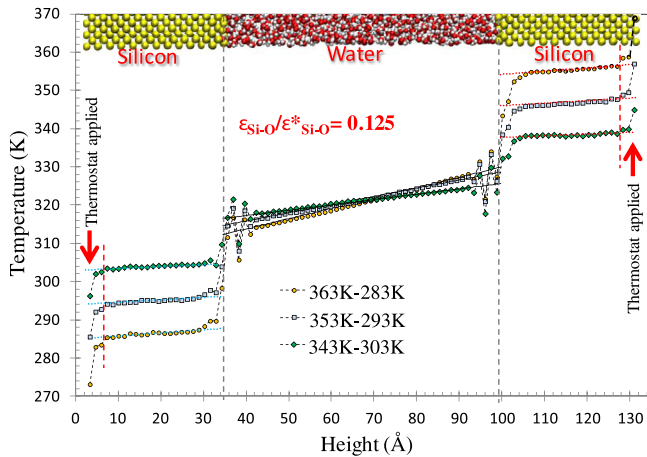


Fig. 7. Temperature profiles of the $0.125 \times \epsilon^*_{\text{Si-O}}$ case with various hot and cold reservoir temperatures.

4. Temperature dependence of ITR

Until now, we clarified that ITR strongly depends on the near surface water density structure, which is a function of $\epsilon_{\text{Si-O}}$ value. Therefore we need to identify the proper parameters for water–silicon interactions. For this purpose, we conducted a nano water droplet study where we characterized the interaction parameters by matching the microscopic wetting behavior of water on silicon with the macroscopic experimental measurements [31]. Fig. 6a–e shows the snapshots of the nano-scale droplets formed on bare (1,0,0) silicon surface and the microscopic contact angle values for the 0.4, 0.2, 0.125, 0.1 and 0.05 $\times \epsilon^*_{\text{Si-O}}$ values. Increase of interaction strength decreases the contact angle so that the wettability changes from low to high in the studied range. By considering the line tension effects creating deviations between the nano-scale contact angle and the macro-scale value, an appropriate estimate for the interaction strength value was found as $\epsilon_{\text{Si-O}} = 0.125 \times \epsilon^*_{\text{Si-O}}$ which recovers the experimental macroscopic contact angle of water on pure silicon surface as 88° [31]. Details of this result and the methodology for calculation of the line tension effects to relate the wetting angles of nano-scale and macroscopic droplets can be found in Ref. [31].

Using the proper interaction strength value of $\epsilon_{\text{Si-O}} = 0.125 \times \epsilon^*_{\text{Si-O}}$, we investigated the temperature dependency of

L_K at water–silicon interface. For this purpose, we assigned different temperature values on the hot reservoir as 363, 353 and 343 K while the cold reservoir was kept at 283, 293 and 303 K, respectively. Temperature profile for each case is shown in Fig. 7. As the temperature difference assigned through the heat baths decreases, resulting heat flux values are decreased. The calculated L_{K-H} , L_{K-C} , heat flux, temperature gradients and thermal conductivity of liquid water are tabulated in Table 3.

Before focusing on the L_K variation at different surface temperatures, we should study the density structures near surface at each different temperature case. Density profiles of silicon–water–silicon system for different temperature differences are given in Fig. 8. While Fig. 8a shows slightly higher density peaks on the cold side for coarse bin (0.0672 nm) results, real behavior can only be characterized with a finer bin size (0.0168 nm) as shown in Fig. 8b. Comparison of water densities near different temperature surfaces through Fig. 8b validates that the near wall water structure shows no dependency on the surface temperature, similar to our earlier results for low wetting surfaces.

Since the near surface water density is independent of the wall temperature, we can now properly characterize the temperature dependency of L_K . Fig. 9 gives the L_K values at different temperature surfaces with the corresponding standard deviations, where lower temperature difference cases exhibit higher fluctuations. Similar to the theoretical predictions, ITR decreases with increased temperature since the phonon density of state is higher at high temperatures, which creates better coupling. Calculated L_K values (≈ 9 nm) are consistent with the experimental measurements, where 6–12 nm L_K values are found for hydrophilic and hydrophobic surfaces [33].

5. Conclusions

We studied temperature dependence of the water/silicon interface thermal resistance with proper emphasize on the surface wetting properties and liquid layering near the surface. Results show that the interface thermal resistance between a liquid and solid is dominated by the liquid structure formed on the surface under high wetting conditions. In such case, change of temperature not only alters the phonon transport, but also creates different coupling between liquid and solid molecules due to the variation of liquid ordering near the surface. As a result, interface resistance increases with increased temperature for high wetting surfaces. The opposite behavior is true for low wetting surfaces, where the

Table 3

Kapitza lengths at hot (L_{K-H}) and cold (L_{K-C}) surfaces, heat flux, temperature gradients and thermal conductivity of liquid water of $0.125 \times \epsilon^*_{\text{Si-O}}$ case.

| Case | T_H & T_C (K) | $\epsilon_{\text{Si-O}}/\epsilon^*_{\text{Si-O}}$ | q_x (W/m ²) | dT/dx (K/Å) | k_{water} (W/K m) | T_H (K) | L_{K-H} (nm) | T_C (K) | L_{K-C} (nm) |
|------|-------------------|---|---------------------------|---------------|----------------------------|-----------|----------------|-----------|----------------|
| 1 | 363–283 | 0.125 | 5.411 | 0.271 | 0.661 | 355.5 | 8.213 | 286.5 | 8.97 |
| 2 | 353–293 | 0.125 | 4.286 | 0.215 | 0.659 | 347 | 8.186 | 295.1 | 8.878 |
| 3 | 343–303 | 0.125 | 2.843 | 0.14 | 0.672 | 338.4 | 8.321 | 303.8 | 8.621 |

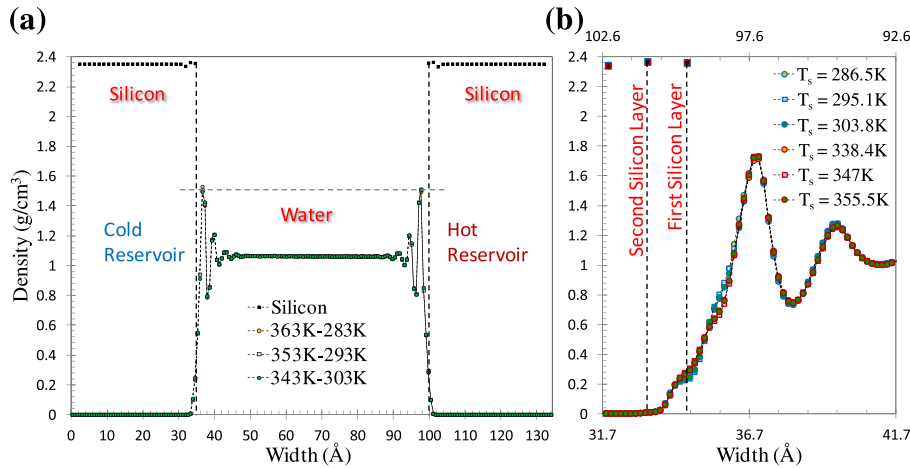


Fig. 8. (a) Density profiles for different temperature cases. (b) Comparison of water distributions near the surfaces at different temperatures.

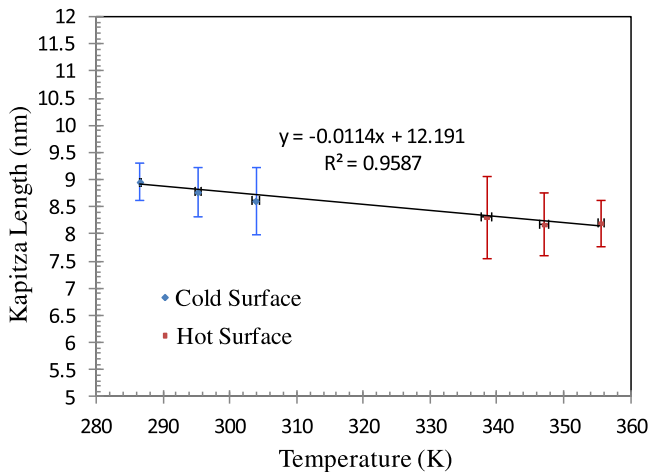


Fig. 9. Variation of L_K with the change in the surface temperature for $0.125 \times \epsilon^*_{\text{si-o}}$ case. Standard deviations of L_K are given as error bars.

density structure near the surface is independent of the surface temperature. As a result, change of surface temperature only affects phonon transport. Similar to the theoretical expectations, interface thermal resistance decreases with increased temperature of a surface with wettability. In the light of these results, the wetting behavior of a liquid/solid couple should be properly considered in order to characterize the behavior of interface thermal resistance. For such cases, we also clarified that the classical mixing rules frequently employed in the literature are not suitable to capture the correct interface behavior. The interaction strength value predicted by the Lorentz–Berthelot mixing rule creates highly hydrophilic silicon surface opposite to the experimental measurements. Hence, by conducting a nano-scale water droplet study, we properly tuned the interaction parameters in order to recover the real hydrophobic nature of bare silicon surface. Using the proper parameters, we characterized the temperature dependence of Kapitza length at the water/silicon interface, where MD predicted Kapitza length values (≈ 9 nm) agree with the experimental results for slightly hydrophobic surfaces.

Acknowledgments

This work was supported by the National Science Foundation under Grant No: CBET 0931988. We would also like to thank the

Extreme Science and Engineering Discovery Environment (XSEDE) supported by the National Science Foundation grant number OCI 1053575 for computing resources through the grant of Dr. Barisik (Grant No: TG-CTS130001).

References

- [1] D.G. Cahill, W.K. Ford, K.E. Goodson, G.D. Mahan, A. Majumdar, H.J. Maris, R. Merlin, S.R. Phillpot, Nanoscale thermal transport, *J. Appl. Phys.* 93 (2003) 793.
- [2] E.T. Swartz, R.O. Pohl, Thermal boundary resistance, *Rev. Mod. Phys.* 61 (1989) 605–668.
- [3] M. Hu, P. Keblinski, P.K. Schelling, Kapitza conductance of silicon–amorphous polyethylene interfaces by molecular dynamics simulations, *Phys. Rev. B* 79 (2009) 104305–110312.
- [4] B.H. Kim, A. Beskok, T. Cagin, Thermal interactions in nanoscale fluid flow: molecular dynamics simulations with solid–liquid interfaces, *Microfluid. Nanofluid.* 5 (2008) 551–559.
- [5] B.H. Kim, A. Beskok, T. Cagin, Molecular dynamics simulations of thermal resistance at the liquid–solid interface, *J. Chem. Phys.* 129 (2008) 174701.
- [6] M. Barisik, A. Beskok, Boundary treatment effects on molecular dynamics simulations of interface thermal resistance, *J. Comput. Phys.* 231 (23) (2012) 7881–7892.
- [7] Z. Shi, M. Barisik, A. Beskok, Molecular dynamics modeling of thermal resistance at argon–graphite and argon–silver interfaces, *Int. J. Therm. Sci.* 59 (2012) 29–37.
- [8] Daichi Torii, Taku Ohara, Kenji Ishida, Molecular-scale mechanism of thermal resistance at the solid–liquid interfaces: influence of interaction parameters between solid and liquid molecules, *J. Heat Transf.* 132 (1) (2009) 012402.
- [9] L. Xue, P. Keblinski, S.R. Phillpot, S.U.-S. Choi, J.A. Eastman, Effect of liquid layering at the liquid–solid interface on thermal transport, *Int. J. Heat Mass Transf.* 47 (2004) 4277–4284.
- [10] L. Xue, P. Keblinski, S.R. Phillpot, S.U.-S. Choi, J.A. Eastman, Two regimes of thermal resistance at a liquid–solid interface, *J. Chem. Phys.* 118 (2003) 337–339.
- [11] K.M. Issa, A.A. Mohamad, Lowering liquid–solid interfacial thermal resistance with nanopatterned surfaces, *Phys. Rev. E* 85 (2012) 031602.
- [12] P.A.E. Schoen, B. Michel, A. Curioni, D. Poulikakos, Hydrogen-bond enhanced thermal energy transport at functionalized hydrophobic and hydrophilic silica–water interfaces, *Chem. Phys. Lett.* 476 (2009) 271–276.
- [13] J.L. Barrat, F. Chiaruttini, Kapitza resistance at the liquid–solid interface, *Mol. Phys.* 10 (2003) 1605–1610.
- [14] J.H. Cha, S. Chiashi, J. Shiomi, S. Maruyama, Generalized model of thermal boundary conductance between SWNT and surrounding supercritical Lennard–Jones fluid – derivation from molecular dynamics simulations, *Int. J. Heat Mass Transf.* 55 (2012) 2008–2013.
- [15] S. Murad, I.K. Puri, Thermal transport across nanoscale solid–fluid interfaces, *Appl. Phys. Lett.* 92 (2008) 133105.
- [16] S. Murad, I.K. Puri, Molecular simulation of thermal transport across hydrophilic interfaces, *Chem. Phys. Lett.* 467 (2008) 110–113.
- [17] S. Murad, I.K. Puri, Thermal transport through a fluid–solid interface, *Chem. Phys. Lett.* 476 (2009) 267–270.
- [18] R.J. Stevens, L.V. Zhigilei, P.M. Norris, Effects of temperature and disorder on thermal boundary conductance at solid–solid interfaces: nonequilibrium molecular dynamics simulations, *Int. J. Heat Mass Transf.* 50 (2007) 3977–3989.

- [19] J.C. Duda, C.J. Kimmer, W.A. Soffa, X.W. Zhou, R.E. Jones, Influence of crystallographic orientation and anisotropy on Kapitza conductance via classical molecular dynamics simulations, *J. Appl. Phys.* 112 (2012) 09351.
- [20] T. Luo, J.R. Lloyd, Enhancement of thermal energy transport across graphene/graphite and polymer interfaces: a molecular dynamics study, *Adv. Funct. Mater.* 22 (2012) 2495–2502.
- [21] J.C. Duda, T.S. English, E.S. Piekos, W.A. Soffa, L.V. Zhigilei, P.E. Hopkins, Implications of cross-species interactions on the temperature dependence of Kapitza conductance, *Phys. Rev. B* 84 (2011) 193301.
- [22] M. Barisik, A. Beskok, Equilibrium molecular dynamics studies on nanoscale confined fluids, *Microfluid. Nanofluid.* 11 (3) (2011) 269–282.
- [23] H.J.C. Berendsen, J.R. Grigera, T.P.J. Straatsma, The missing term in effective pair potentials, *Phys. Chem.* 91 (1987) 6269–6271.
- [24] M.P. Allen, D.J. Tildesley, *Computer Simulation of Liquids*, Oxford Science Publications Oxford University Press, New York, 1989.
- [25] S. Miyamoto, P.A. Kollman, Settle: an analytical version of the shake and rattle algorithm for rigid water models, *J. Comput. Chem.* 13 (1992) 952–962.
- [26] S.J. Plimpton, R. Pollock, M. Stevens, Particle-mesh Ewald and rRESPA for parallel molecular dynamics simulations, in: *Proc of the Eighth SIAM Conference on Parallel Processing for Scientific Computing*, 1997, pp. 8–21.
- [27] F.H. Stillinger, T.A. Weber, Computer simulation of local order in condensed phase of silicon, *Phys. Rev. B* 31 (1985) 5262–5271.
- [28] S.J. Plimpton, Fast parallel algorithms for Short-Range molecular dynamics, *J. Comput. Phys.* 117 (1995) 1–19. See: <http://lammmps.sandia.gov>. for more information.
- [29] J.H. Irving, J.G. Kirkwood, The statistical mechanical theory of transport processes. IV. The equations of hydrodynamics, *J. Chem. Phys.* 18 (1950) 817–829.
- [30] B.D. Todd, P.J. Daivis, D.J. Evans, Heat flux vector in highly inhomogeneous nonequilibrium fluids, *Phys. Rev. E* 51 (1995) 4362–4368.
- [31] M. Barisik, A. Beskok, Wetting characterization of silicon (1,0,0) surface, *Mol. Simulat.* 39 (9) (2013) 700–709.
- [32] H.D. Young, *University Physics*, seventh ed., Addison Wesley, 1992. Table 15-5.
- [33] Z. Ge, D.G. Cahill, P.V. Braun, Thermal conductance of hydrophilic and hydrophobic interfaces, *Phys. Rev. Lett.* 96 (2006) 186101.